Acta Biomaterialia 49 (2017) 575–589

Contents lists available at ScienceDirect

Acta Biomaterialia

journal homepage: www.elsevier.com/locate/actabiomat

Full length article

Harnessing Wharton's jelly stem cell differentiation into bone-*like* nodule on calcium phosphate substrate without osteoinductive factors

S. Mechiche Alami [a,b,1], H. Rammal [a,b,1], C. Boulagnon-Rombi [c], F. Velard [a,b], F. Lazar [d], R. Drevet [d], D. Laurent Maquin [a,b], S.C. Gangloff [a,e], J. Hemmerlé [f], J.C. Voegel [f], G. Francius [g], P. Schaaf [f,h,i,j], F. Boulmedais [h], H. Kerdjoudj [a,b,*]

[a] *EA 4691, Biomatériaux et Inflammation en Site Osseux (BIOS), SFR-CAP Santé (FED 4231), Université de Reims Champagne Ardenne, Reims, France*
[b] *UFR d'odontologie, Université de Reims Champagne Ardenne, Reims, France*
[c] *Laboratoire d'anatomie et cytologie pathologique, Centre Hospitalo-Universitaire, Hôpital Robert Debré, Reims, France*
[d] *EA 4695, Laboratoire d'Ingénierie et Sciences des Matériaux (LISM), Université de Reims Czampagne Ardenne, Reims, France*
[e] *UFR de Pharmacie, Université de Reims Champagne Ardenne, Reims, France*
[f] *INSERM, UMR-S 1121, "Biomatériaux et Bioingénierie", Faculté de Chirurgie Dentaire, Université de Strasbourg, Strasbourg, France*
[g] *CNRS, UMR 7564, Laboratoire de Chimie Physique et Microbiologie pour l'Environnement (LCPME), Université de Lorraine, Nancy, France*
[h] *Institut Charles Sadron, Centre National de la Recherche Scientifique, Université de Strasbourg, Starsbourg, France*
[i] *University of Strasbourg Institute of Advanced Study, Strasbourg, France*
[j] *Institut Universitaire de France, Paris, France*

ARTICLE INFO

Article history:
Received 20 June 2016
Received in revised form 11 November 2016
Accepted 17 November 2016
Available online 22 November 2016

Keywords:
Calcium phosphate
Wharton's jelly stem cells
Bone regeneration
Bone-*like* nodule
Osteogenic factors free

ABSTRACT

An important aim of bone regenerative medicine is to design biomaterials with controlled chemical and topographical features to guide stem cell fate towards osteoblasts without addition of specific osteogenic factors. Herein, we find that sprayed bioactive and biocompatible calcium phosphate substrates (CaP) with controlled topography induce, in a well-orchestrated manner, Wharton's jelly stem cells (WJ-SCs) differentiation into osteoblastic lineage without any osteogenic supplements. The resulting WJ-SCs commitment exhibits features of native bone, through the formation of three-dimensional bone-*like* nodule with osteocyte-like cells embedded into a mineralized type I collagen. To our knowledge, these results present the first observation of a whole differentiation process from stem cell to osteocytes-like on a synthetic material. This suggests a great potential of sprayed CaP and WJ-SCs in bone tissue engineering. These unique features may facilitate the transition from bench to bedside and the development of successful engineered bone.

Statement of Significance

Designing materials to direct stem cell fate has a relevant impact on stem cell biology and provides insights facilitating their clinical application in regenerative medicine. Inspired by natural bone compositions, a friendly automated spray-assisted system was used to build calcium phosphate substrate (CaP). Sprayed biomimetic solutions using mild conditions led to the formation of CaP with controlled physical properties, good bioactivity and biocompatibility. Herein, we show that via optimization of physical properties, CaP substrate induce osteogenic differentiation of Wharton's jelly stem cells (WJ-SCs) without adding osteogenic supplement factors. These results suggest a great potential of sprayed CaP and WJ-SCs in bone tissue engineering and may facilitate the transition from bench to beside and the development of clinically successful engineered bone.

1. Introduction

Bone tissue regeneration remains a significant and challenging endeavour in the field of orthopaedic and craniofacial surgery. Bone has a remarkable ability for healing and represents the only

* Corresponding author at: EA 4691, «Biomatériaux et Inflammation en Site Osseux», Pôle Santé, UFR d'odontologie, SFR-CAP Santé (FED 4231), URCA, 1 Avenue du Maréchal Juin, 51100 Reims, France.
E-mail address: halima.kerdjoudj@univ-reims.fr (H. Kerdjoudj).
[1] Both authors have contributed equally to this work.

http://dx.doi.org/10.1016/j.actbio.2016.11.042
1742-7061/

connective tissue that retains the ability to enlist all of the key prenatal signalling events during healing. However it cannot heal by regeneration if an injury is beyond a critical limit. Despite progresses in clinical treatments in recent years, several drawbacks exist such as risk of donor site morbidity for autografts harvest, pathogen transmission and rejection by the recipient's body in case of either allografts and xenografts use, and poor osteoinductive and mechanical features of synthetic ceramics. Bone morphogenetic proteins (BMPs) have been employed in many preclinical and clinical studies exploring their osteoinductive potential in several animal models and human diseases. The initial excitement arising from the excellent clinical results of bone morphogenetic protein-2 (BMP-2) has been tempered significantly by increasing safety and cost concerns [1].

To promote *in vivo* bone formation, bone tissue engineering approaches involve the combination of stem cells (SCs) and bioactive materials [2]. Adult SCs are involved in tissue regeneration throughout a person's life. Major bottlenecks in the use of adult SCs are their highly invasive harvesting procedure, low frequency and age-declining proliferation and differentiation potential. Therefore, the search for alternative sources for adult SCs is of significant value. So far, increasing success has been reported in the literature for isolation and characterization of stem cells from perinatal tissues as Wharton's jelly [3–5]. Wharton's jelly stem cells (WJ-SCs) are thought to constitute powerful candidates for regenerative medicine and driving them into the osteoblastic lineage represents a great promise for regenerating bone.

Desired bioactive materials would promote SC differentiation without any additional growth factors [6,7]. Often, biochemists induce SCs differentiation by adding chemical factors *in vitro* such as dexamethasone or β-glycerophosphate, which are not encountered in the body. Recent innovative discoveries suggest the importance of intrinsic mechanical (elastic modulus) and biophysical properties of substrate (topography), in eliciting cellular effects compared to the traditional induction method using medium supplements that are not physiologically relevant [8,9]. Among the numerous attempts to develop bone tissue interactive substrates, calcium phosphate (CaP) ceramics, obtained by either wet-chemical deposition (sol-gel, biomimetics…) or physical deposition (plasma spray), have received wide attention due to their similarities with the inorganic mineral phase of bone [10,11]. However, limitations regarding harsh fabrication conditions, long-term stability and biocompatibility, and the requirement of expensive instruments, with respect to these coating techniques still exist. Moreover, the poor osteoinductive properties of these materials can lead to failure of the stem cell osteoblastic commitment [7].

On the basis of the bone structure, it is assumed that optimal osteoinductive coatings should possess several types of features as a rough surface, high stiffness strength close to that of the bone. Recently, a new and straightforward method based on spray-assisted deposition was used to design a bone inspired substrate [12]. This versatile method allows the construction of submicron-sized coatings with possible modulation of thickness and surface topography. The ease of adapting this spray technology in industrial production presents an additional advantage. Our hypothesis is that the intrinsic mechanical and biophysical properties of sprayed CaP are able to induce osteogenic differentiation and could be used as a substrate for bone tissue engineering. Here, we examine the effect of CaP substrate on WJ-SCs behaviour through cell mechanobiology and integrin expression. To our knowledge, for the first time, we demonstrate the *in vitro* sequences of WJ-SCs proliferation, differentiation and mineralization associated with three-dimensional bone-*like* nodule formation without any biochemical supplements.

2. Materials and methods

2.1. Material

Calcium nitrate ($Ca(NO_3)_2$,$4H_2O$), diammonium hydrogen phosphate ($(NH_4)_2{\cdot}HPO_4$) and Tris(hydroxymethyl) aminomethane (Tris) from Sigma were used without further purification. The salt solutions were prepared in ultrapure water (Millipore®). Calcium solution of $Ca(NO_3)_2{\cdot}4H_2O$ (0.32 M) and a phosphate solution of $(NH_4)_2$ $HPO_4{\cdot}$(0.2 M) were prepared in Tris buffer (10 mM Tris, pH 4 and pH 10 respectively). Coverslips glass of 14 mm diameter were provided from Thermo Scientific. Each experiment was preceded by a cleaning step of the coverslip glass with sodium dodecyl sulfate (100 mM, Sigma) for 15 min at 100 °C. After an intensive ultrapure water (Millipore®) rinse, coverslips were brought in contact with hydrochloric acid (100 mM, Sigma) for 15 min at 100 °C and finally rinsed with ultrapure water and conserved at 4 °C.

2.2. Substrate build-up

An automated spraying device was used for calcium phosphate (CaP) build-up. This device is constituted of four identical Airbrushes VL (Paasche®, USA) nozzles. Each nozzle is pressurized by in-house compressed air line under a pressure of 1 bar and connected to solenoid valves. The spraying of the different solutions, following a chosen deposition sequence, is obtained by a succession of closings and openings of the valves controlled by homemade software. Three nozzles allow spraying of the calcium, the phosphate, and of the rinsing solutions. The fourth nozzle, free of solution, is used for the drying step. The cleaned coverslip is mounted vertically on a mobile holder. For homogenous build-up of CaP substrate, the holder was rotated at 150 rpm. For the build-up of calcium phosphate, both calcium and phosphate solutions were sprayed simultaneously, on coverslip glass, for 2 s followed by a rinsing step of 2 s with ultrapure water and a drying step of 2 s under compressed air. To get the desired coated surfaces, these steps were repeated 50, 100 and 150 times and the resulting substrates were respectively denominated CaP_{50}, CaP_{100} and CaP_{150}. The surface morphology and chemical composition were respectively determined by scanning electron microscopy (SEM, JEOL JSM 6010LA) and X-ray diffractometer (DRX, Bruker D8 Advance). The X-ray pattern data was collected from $2\theta = 20°$ to 45° using a monochromatic Cu $_{K\alpha}$ radiation with a step of 0.04° every 12 s.

2.3. Bioactivity experiments

CaP substrates were soaked in 1 mL of Dulbecco's Modified Eagle Medium (DMEM, Gibco, 10566016) at 37 °C. After 15 min, 30 min, 1 h, 2 h, 4 h, 24 h and 48 h of incubation, the substrates were retrieved and the serum free DMEM was collected to assess the calcium and phosphorus ions using Induced Coupled Plasma – Optical Emission Spectroscopy (ICP-OES, iCAP 6300 duo plasma emission spectrometer) [13]. Each point of time was analysed in triplicate.

2.4. Substrate characterization

CaP substrates before and after immersion in DMEM supplemented with fetal bovine serum (FBS) for 24 h were investigated by scanning electron microscopy-energy dispersive X-ray spectroscopy (SEM-EDX, JEOL JSM 6010LA). The X-ray spectra were acquired at primary beam energy of 10 keV with an acquisition time of 30 s. X-ray maps were obtained by scanning large areas

(68 × 54 μm) of three different areas. Each analysis was performed in triplicate.

The spectra relative to the CaP substrate were also determined by near infrared confocal Raman spectrometer (Labram ARAMIS, Horiba Jobin Yvon S.A.S., France) coupled to a microscope (Olympus, BX41, France) using excitation source at 785 nm and by the Attenuated Total Reflection (ATR) mode using a diamond ATR accessory-Fourier Transform Infrared spectrometer (FTIR, Vertex 70 spectrometer, Bruker, Germany) using DTGS detector.

The surface topography of CaP substrates was observed by atomic force microscopy (AFM, MFP3D-BIO instrument) in contact mode and both in air and aqueous medium in wet conditions (DMEM without phenol red) at room temperature. The applied force between the tip and the surface was carefully monitored and minimized at about 0.25 nN, and all images were collected with a resolution of 512 × 512 pixels and a scan rate of 1 Hz. The nanoindentation method provides the Young's modulus calculated from the force vs. indentation curve. Triangular cantilevers were purchased from Bruker (MLCT, Bruker-nano AXS). The spring constants of the cantilevers were calculated in the range of 12–16 pN/nm using the thermal noise method. Maps of mechanical properties (FVI for Force Volume Image) were obtained by recording a grid map of 50-by-50 force curves at different locations of 80 × 80 μm on the samples. The maximum loading force was 5 nN. Maps of mechanical and adhesive properties and the corresponding histograms (statistical distribution) were estimated from the analysis of the approach curves according to the Sneddon model [14] within the framework of Sneddon theory, the loading force F depends on the indentation depth δ according to:

$$F = \frac{2E \cdot \mathrm{Tan}(\alpha)}{\pi(1-\nu^2)}\delta^2 f_{\mathrm{BECC}}$$

where δ is the indentation depth, ν the Poisson coefficient, α is the semi-top angle of the tip and f_{BECC} is the Bottom Effect Cone Correction function that takes into account the stiffness of the film-supporting substrate [15]. FVI were performed at 0.5 Hz scan rate and with maximal loading/pulling speed of about 2 μm/s. Then, they were analyzed by means of an automatic Matlab algorithm described elsewhere [16]. Briefly, the physicochemical parameters involved in Sneddon model [14] were estimated from the raw data using a nonlinear regression procedure. The method used was based on advanced tools for "segmenting" the force curves *i.e.*, automatically detecting the tip-to-surface contact point with accuracy.

2.5. Wharton's jelly stem cells

Human umbilical cord harvesting was approved ethically and methodologically by our local Research Institution and was conducted with informed patients (written consent, non-opposition) in accordance with the usual ethical legal regulations (Article R 1243-57). All procedures were done in accordance with our authorization and registration number DC-2014-2262 given by the National "Cellule de Bioéthique". Wharton's jelly stem cells (WJ-SCs) were enzymatically isolated from fresh human umbilical cords obtained after full-term births according to Mechiche Alami et al. [17]. WJ-SCs were amplified at density of 3 × 10^3 cell/cm^2 in α-MEM culture medium (Lonza, catalog number # BE12-169F) supplemented with 10% decomplemented FBS, 1% Penicillin/Streptomycin/Amphotericin B and 1% Glutamax® (*v/v*, Gibco) and maintained in a humidified atmosphere of 5% CO_2 at 37 °C with a medium change every two days. At 3rd passage, WJ-SCs were characterized by flow cytometry (FACSCalibur; BD Bioscience) through the expression of CD73, CD90, CD44, CD105, CD34, CD45 and HLA-DR and then used in our experimental procedure at the 4th passage. WJ-SCs were seeded in 24 well plates at 24,000 cells/cm^2 on UV-decontaminated CaP substrates. UV-decontaminated coverslip glass was used as control. Cells were maintained in α-MEM culture medium and the culture medium was changed every two days until 28 days.

2.6. Cytoskeleton-vinculin staining

After five days of culture on CaP and coverslip glass, WJ-SCs were fixed in 4% (*w/v*) paraformaldehyde (Sigma-Aldrich) at 37 °C for 10 min. Cells were then permeabilized with 0.5% (*v/v*) Triton X-100 for 15 min and blocked in 3% (*v/v*) bovine serum albumin (BSA) (Sigma-Aldrich) in DPBS for 1 h at room temperature. After being blocked, the cells were incubated overnight with a mouse polyclonal antibody targeting vinculin (US-Biological, catalog number # 135223) at a 1:25 dilution in blocking buffer. After two rinses with DPBS, a secondary anti-mouse biotinylated antibody (Invitrogen) was used at a 1:50 dilution for 30 min at room temperature followed by Alexa® 594-conjugated streptavidin at 1:200 dilution (Invitrogen, catalog number # S11227) for 30 min at room temperature. Alexa® 488-phalloidin (1:100 dilution in 0.1% Triton X-100) was used to stain F-actin for 45 min at room temperature. Nuclei were counter-stained with 4,6-diamidino-2-phenylindole (DAPI, 100 ng/mL, 1:10,000 dilution) for 5 min. The stained cells were mounted and imaged by fluorescence microscopy (Zeiss microscopy, ×63 oil immersion objective).

2.7. Integrin α2 and β1 immuno-labeling

After five days of culture on CaP and coverslip glass, fixed and permeabilized WJ-SCs were prepared as previously. After being blocked, the cells were incubated overnight with a mouse monoclonal antibody targeting α2 or β1 integrin subunits (Santa Cruz Biotechnology catalog number # J1006 and B2411, respectively) at a 1:100 dilution in blocking buffer. After two rinse with DPBS, a secondary rabbit anti-mouse IgG biotinylated antibody (Invitrogen) was used at a 1:100 dilution for 30 min at room temperature followed by Alexa® 488-conjugated streptavidine at 1:200 dilution (Invitrogen catalog number # S11223) for 30 min at room temperature. Nuclei were counter-stained with DAPI. The stained cells were mounted and imaged by fluorescence microscopy (Zeiss microscopy, ×20 objective).

2.8. Wharton's jelly stem cell stiffness

After five days of culture on CaP and coverslip glass, WJ-SCs were fixed in 1% (*w/v*) paraformaldehyde at 37 °C for 10 min. Cell topography and cell stiffness were followed by atomic force microscopy (AFM, MFP3D-BIO instrument) as previously described.

2.9. DNA quantification

After 7, 14 and 21 days of culture on CaP and coverslip glass, DNA of WJ-SCs was extracted using MasterPure™ DNA Purification Kit (*Epicentre® Biotechnologies*, France) in accordance with the manufacturer protocol. Extracted DNA was assessed by measuring the absorbance at 260 and 280 nm (Nanodrop®, Thermo Scientific) with 260/280 nm absorbance ratio for all measured samples comprised between 1.8 and 2.

2.10. Scanning electron microscopy

After 7, 14 and 21 days of culture on CaP and coverslip glass, WJ-SCs were fixed in 2.5% (*w/v*) glutaraldehyde (Sigma-Aldrich) at room temperature for 1 h. Cells were dehydrated in graded ethanol solutions from 50 to 100% and in hexamethyldisilazane (HMDS, Sigma) for 10 min. After air-drying at room temperature, samples

were sputtered with a thin gold–palladium film under a JEOL ion sputter JFC 1100. Cells were viewed using a LaB6 electron microscope (JEOL JSM-5400 LV).

2.11. Alkaline phosphatase activity

After 7, 14 and 21 days of culture on CaP and coverslip glass, WJ-SCs were fixed in 4% (*w/v*) paraformaldehyde at 37 °C for 15 min then incubated with Alkaline Phosphatase Substrate (SigmaFast BCIP/NBT, Sigma-Aldrich) at room temperature for 15 min. Purple color development was imaged using EvosXL optical microscope (Life Technologies, ×20 magnification).

2.12. Quantitative real time polymerase chain reaction (qRT-PCR)

After 7, 14 and 21 days of culture on CaP and coverslip glass, total RNAs of WJ-SCs were extracted using MasterPure™ RNA Purification Kit (*Epicentre® Biotechnologies*) in accordance with the manufacturer protocol. RNA purity was assessed by measuring the absorbance ratio at 260/280 nm (Nanodrop 2000C, Thermo Scientific) comprised between 1.8 and 2. RNA (500 ng) were reverse transcribed into cDNA using a High Capacity cDNA Reverse Transcription kit (Applied Biosystems) following manufacturer instructions. cDNA product was amplified by qRT-PCR on a StepOne Plus™ system (Applied Biosystems). Using this approach, the mRNA levels of BGLAP and RPS18 were determined using the double strand-specific Power SYBR® Green dye system (Applied Biosystems), the mRNA levels of CFOS, CMYC, SPP1, COL1A1 and RPS18 were determined using Fast SYBR® Green Master Mix and the mRNA levels of RUNX-2 and ALPL (Table 2) were determined using Taqman® Fast Advanced Master Mix. Reactions using Power SYBR® Green dye system were performed according to a thermal profile that corresponds to 40 cycles of denaturation at 95 °C for 15 s, annealing and extension at 60 °C for 1 min. Reactions using the Fast SYBR® Green Master Mix system were performed according to a thermal profile that corresponds to 40 cycles of denaturation at 95 °C for 3 s, annealing and extension at 60 °C for 30 s. Data collection was performed at the end of each annealing/extension step. The third step that consists in a dissociation process is performed to ensure the specificity of the amplicons by measuring their melting temperature (Tm). Reactions using Taqman® Fast Advanced Master Mix systems were performed according to the same thermal profile used for Power SYBR® Green dye system without the dissociation process step. Data analysis was performed with the StepOne™ Software *v*2.3 (Applied Biosystems). Relative expression was calculated using the $2^{-\Delta\Delta Ct}$ method with RPS18 as the reference gene.

Table 1
Atomic force microscopy and force analyses.

	CaP 50	CaP 100	CaP 150
Thickness (μm)	1.3 ± 0.52	2.7 ± 0.74	4.2 ± 1.39
Roughness (nm)	374 ± 191	458 ± 263	773 ± 322
Stiffness (kPa)	6457 ± 1987	5130 ± 1439	5863 ± 2013

2.13. Histology and immunohistochemistry

After 28 days of culture on CaP, WJ-SCs were fixed in 4% (*w/v*) paraformaldehyde overnight and dehydrated in solutions with gradually increasing concentration of ethanol content. Subsequently, the samples were embedded in paraffin, cut into 4 μm sections (rotation microtome RM2055, Leica Microsystems). Hematoxylin-Eosin-Saffron (HES) and Masson's trichrome staining were performed separately on consecutive tissue sections and images were taken using scanner iScan Coreo AU (Roche®, Ventana). For immunohistochemistry, after deparaffinization, 4 μm sections were incubated with the Cell Conditioner 1 (EDTA, pH 8.4) for 64 min, followed by preprimary peroxidase inhibition and incubation with the primary antibody anti-cleaved caspase 3 (Rabbit polyclonal, Cell signaling technology, catalog number # 9661) at a 1:600 dilution at 37 °C for 32 min on the automated staining instrument BenchMark XT (Ventana Medical System). Then, the staining reaction was performed using the UltraView Universal DAB v3 Kit (Ventana Medical System). The counter-stain and post-counter-stain comprised Haematoxylin and bluing reagent. Images were taken using scanner iScan Coreo AU.

2.14. Transmission electron microscopy

After 28 days of culture on CaP, WJ-SCs were rinsed with 125 mM cacodylate buffer solution, fixed in a mixture of 2% paraformaldehyde and 2.5% glutaraldehyde in 50 mM cacodylate buffer at pH 7.4 for 2 h at room temperature and finally post-fixed in 1% osmium tetroxide in 125 mM cacodylate buffer for 30 min after an overnight incubation in 125 mM cacodylate buffer at 4 °C. Samples were dehydrated in solutions with gradually increasing concentration of ethanol content (from 50, 70, 95, and 100% three times) for 15 min. Samples were embedded in epoxy resin (48.2% epon 812, 34% anhydride nadic methyl, 16.4% anhydride [2-dodecenyl] succinic, and 1.5% 2,4,6-tris dimethylaminoethyl] phenol) for 48 h at 60 °C. After resin polymerization, a heat shock in liquid nitrogen was first performed to remove the substrate. To obtain transversal sections of embedded samples, the cutting surface was reoriented by preparing small block using a circular saw (Bronwill Scientific) and sticking them on new ones. Ultra-thin cross sections (100 nm in thickness) were performed using an automatic ultra-microtome (Ultracut-E Ultramicrotome, Reichert Jung). The specimen was observed with a transmission electron microscope EM208 (FEI Compagny, Philips) operating with an accelerating voltage of 70 kV. Images were captured on SO163 Kodak films.

2.15. High-resolution TEM/electron diffraction

High resolution transmission electron micrographs and selected area electron diffraction patterns were obtained by using a Philips

Table 2
The sequences of the primers used are listed in the table below.

Human gene labelling	Forward primer	Reverse primer
CMYC	GCT-GCT-TAG-ACG-CTG-GAT-TT	TAA-CGT-TGA-GGG-GCA-TCG
CFOS	ACT-ACC-ACT-CAC-CCG-CAG-AC	CCA-GGT-CCG-TGC-AGA-AGT
SPP1	GAG-GGC-TTG-GTT-GTC-AGC	CAA-TTC-TCA-TGG-TAG-TGA-GTT-TTC-C
BGLAP	TGA-GAG-CCC-TCA-CAC-TCC-TC	ACC-TTT-GCT-GGA-CTC-TGC-AC
RPS18	TGC-GAG-TACT-CAA-CAC-CAA-CA	GCA-TAT-CTT-CGG-CCC-ACA
COL1A1	GGG-ATT-CCC-TGG-ACC-TAA-AG	GGA-ACA-CCT-CGC-TCT-CCA-G
RUNX-2	Reference: Hs00231692_m1	
ALPL	Reference: Hs01029144_m1	

CM 200 (Eindhoven) microscope operating with an acceleration voltage of 200 kV.

2.16. Statistical analysis

All statistical analyses were performed using StatXact 7.0, Cytel Inc. ICP-OES measurements were performed in triplicate, with three replicates per sample. Data are presented as mean ± SD (Pairwise comparisons were performed using one-factor ANOVA with Fisher correction). All biological experiments were performed with six independent umbilical cords. Curves represent mean ± SEM (Mann & Withney). qRT-PCR results of SPP1, COL1A1, RUNX-2, ALPL and RPS18 are presented as median (Mann & Withney). For each test a value of $p < 0.05$ was accepted as statistically significant p (rejection level of the null-hypothesis of equal means).

3. Results and discussion

The CaP substrates were prepared at room temperature by simultaneous spraying of $Ca(NO)_3$, $4H_2O$ and $(NH_4)_2HPO_4$ aqueous solutions on a glass coverslip for 2 s followed by a 2 s spraying of the rinsing solution followed by 2 s of drying. This was repeated 50, 100 and 150 times to get three coated surfaces (CaP_{50}, CaP_{100} or CaP_{150}). Chemical and physical properties of these coatings, including homogeneity, calcium phosphate phase and their bioactivity, elastic modulus and surface topography, constitute critical parameters for cell biocompatibility. Therefore, the surface features were first characterized.

3.1. Physico-chemical characterization of CaP substrates

After 50 cycles of simultaneous spray, the glass coverslip appears covered with a thin and homogenous layer of inorganic phase. Scanning electron microscopy (SEM) images of CaP substrate morphology showed spherical aggregates, which increased in size and thickness with the number of spray cycles (50, 100 and 150) (Fig. 1A and B). CaP can exist in several phases, including α- and β-tricalcium phosphate, tetracalcium phosphate, octacalcium phosphate (OCP), dicalcium phosphate dihydrate (DCPD) and hydroxyapatite (HAp) [18]. Among them, HAp is chemically the most similar to CaP in mature bone [19], whereas OCP, a transient precursor of biological apatite, is found in newly formed bone and *in vitro* culture [20]. X-ray maps, obtained by scanning electron microscopy-energy dispersive X-ray spectroscopy (SEM-EDX), showed homogeneous distribution of calcium and phosphorous all over the CaP coatings with an atomic ratio of 1.23 ± 0.02 (Fig. 1C). X-ray diffractometry (XRD), Fourier transform infrared spectroscopy (FTIR) and confocal Raman spectroscopy analysis are given in Figs. 1D, 2A and B (blue lines). XRD is widely used for apatite characterization, since it provides data concerning the crystal structure of a mineral and its composition in the case of mixtures, however, it is not convenient for example to determine amount of hydroxyl groups in calcium phosphate. FTIR and Raman spectroscopy, in many cases are more sensitive than XRD when determining the presence of new phases in particular in low amounts. According to the CaP joint committee on powder diffraction standards (JCPDS) patterns, the XRD pattern showed that the sprayed CaP is composed of HAp with typical diffraction peaks at $2\theta = 10.8°$, 25.88°, 28.97°, 31.77°, 32.20°, 32.90° and of DCPD with diffraction peaks at $2\theta = 11.68°$, 29.44°, 29.94° (Fig. 1D). On FTIR spectra, the main vibration bands are observed at 1021 cm^{-1} (P-O stretching mode of ν3 PO_4), 960 cm^{-1} (P–O stretching mode of ν1 PO_4^{3-}) and 880 cm^{-1} (P-OH stretching mode of HPO_4). The first peak is attributed to nonstoichiometric HAp and the last peak to DCPD phase [21–23]. The peak at 1650 cm^{-1} corresponds to the bending mode of ν2 lattice water molecule of the adsorbed water (Fig. 2A blue line). Finally, Raman spectroscopy showed also typical HAp vibrations [24] (with HAP characteristics peaks: ν_1 PO_4^{3-} vibrations at 962 cm^{-1}, phosphate ν_4 vibrations at 595 cm^{-1} and phosphate ν_3 vibrations at 1074 cm^{-1}) (Fig. 2B blue line).

The bioactivity of CaP has been attributed to different factors, among them the ability of CaP to modulate extracellular calcium and phosphate ions [7]. Indeed, CaP ceramics are known to have dissolution rates under-saturated conditions, which means that they are unstable in long-term culture [25]. Thus, calcium and phosphorus concentrations were determined after 15 min, 30 min, 1 h, 2 h, 4 h, 24 h and 48 h of CaP_{50} immersion in serum-free culture medium (DMEM) by inductively coupled plasma – optical emission spectroscopy (ICP-OES). For both CaP_{100} and CaP_{150} substrates, calcium and phosphorus concentrations are not measured because of detachment of the substrates from the coverslip. Instead of being released, calcium and phosphorus ions from the medium seemed to be adsorbed or incorporated on the CaP_{50} matching with several published works [7]. After 24 h, significant reduction by 50% and 40% for calcium and phosphorus ions, respectively in the medium is observed in comparison to the initial medium (Fig. 2C). As a control, we followed the same concentrations for a glass coverslip where the concentration of both ions stayed fairly constant with the incubation times. The decrease in ions concentration in the medium could be attributed to the precipitation of CaP, which could enhance the adsorption of serum constituents on the surface of the substrate [25,26]. After 24 h of incubation of CaP_{50} in serum-containing DMEM, SEM images of CaP_{50} coating showed an increase in the density of crystal of calcium phosphate on the surface. The quantitative analysis from SEM-EDX showed an increase in Ca/P atomic ratio up to 1.34. Thus, the adsorption of both ions from the medium seems to lead to new calcium phosphate crystallization (Fig. S1 supporting information). A small shoulder at 1115 cm^{-1} appeared on the phosphate region of the FTIR spectra. This is assigned to poorly crystalline hydroxyapatite. Newly FTIR bands appearing at 1640 cm^{-1} (amide I, mainly C═O stretching vibrations) and 1535 cm^{-1} (amide II, the coupling of bending vibration of N—H and stretching vibration of C—N) are characteristic for proteins. The peak present at 1460–1380 cm^{-1} corresponds to CH_2 and CH_3 bands from lipid acyl chains (Fig. 2A red line). The Raman spectra confirmed the formation of apatite and showed the adsorption of constituents from the culture media with prominent protein bands at 1595 cm^{-1} (amide I) and 1377 cm^{-1} (amide III) and lipid peaks at 733 cm^{-1} (C—C stretching) and 1470 cm^{-1} (CH_2 deformation) (Fig 2B, red line).

The thickness, roughness and stiffness of CaP_{50}, CaP_{100} and CaP_{150} substrates soaked in DMEM are assessed by atomic force microscopy (AFM). After scratching, the thickness of substrates is estimated by subtracting the mean height of the scratched area from the mean height of the unscratched one (Fig. 3). The thickness of CaP increased with the number of cycles; from 1.3 ± 0.52 to 4.2 ± 1.3 μm for CaP_{50} and CaP_{150}, respectively. The roughness of the substrate, in terms of quadratic rugosity (Rq), increased with the number of cycles from 374 ± 191 nm to 774 ± 322 nm for CaP_{50} and CaP_{150} respectively (Table 1). Elastic moduli of CaP_{50}, CaP_{100} and CaP_{150} substrates were measured by nanoindentation experiments with AFM. Values on Table 1 showed that the elastic moduli seem to be quite constant for all sprayed CaP (around 6 GPa), which lies in the domain of human bone (cortical bone: 20 GPa and trabecular bone: 2 GPa) [27].

Development of bone-*like* coatings often requires high bioactivity and cortical bone-*like* tensile properties [18]. For example, in the oral and maxillofacial area, an artificial barrier membrane is suggested to seal off the bone defect for a regeneration period of up to several weeks. Some sensitive materials including bioactive

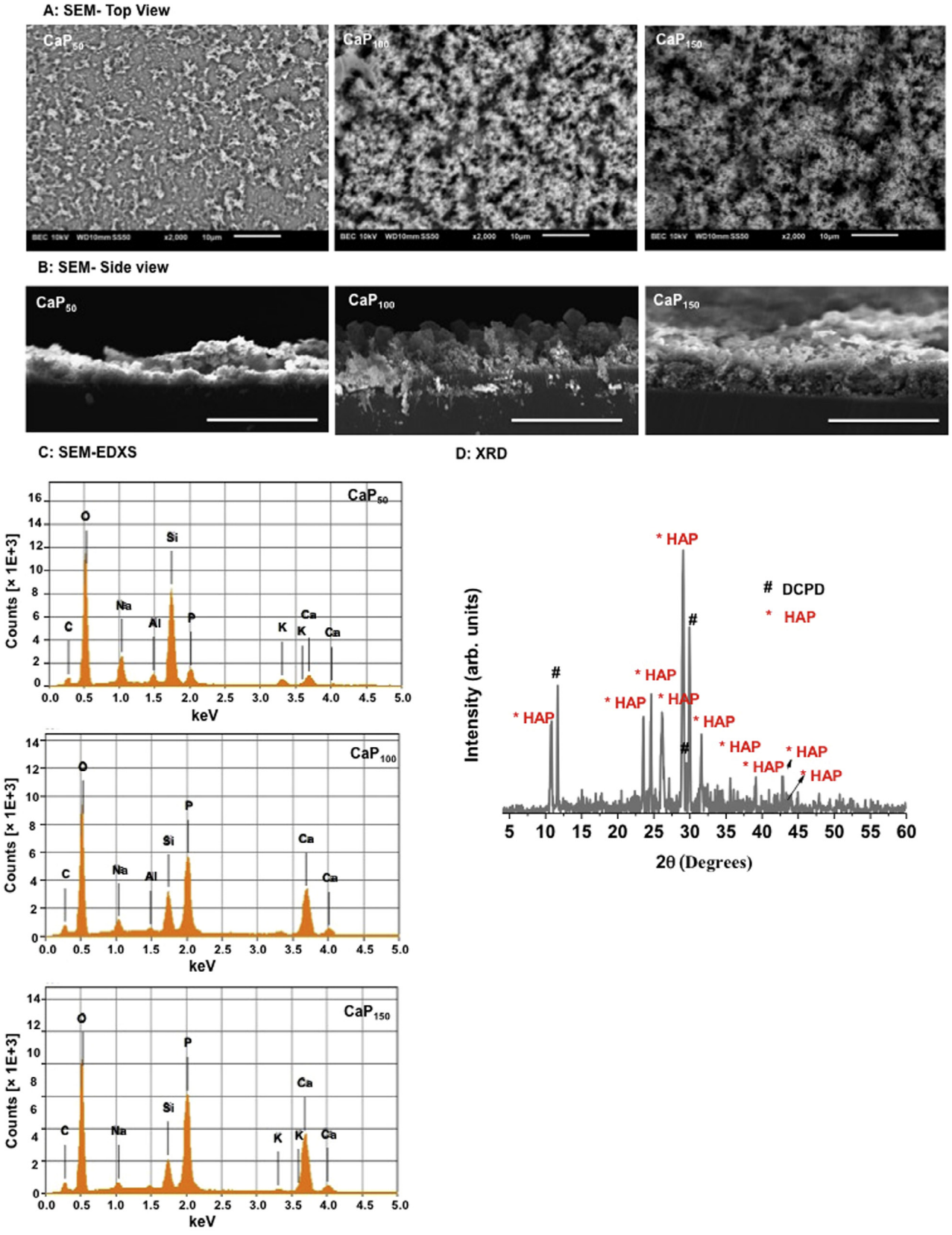

Fig. 1. Surface features and chemical composition. A and B: top and side views of representative scanning electron microscopy. Scale bars indicate 10 μm. C: Spectra obtained by scanning electron microscopy-energy dispersive X-ray spectroscopy (SEM-EDXS), obtained by scanning large areas (68 × 54 μm) of three different areas of each sample. Each analysis was performed in triplicate. D: Pattern of X-ray diffraction (XRD).

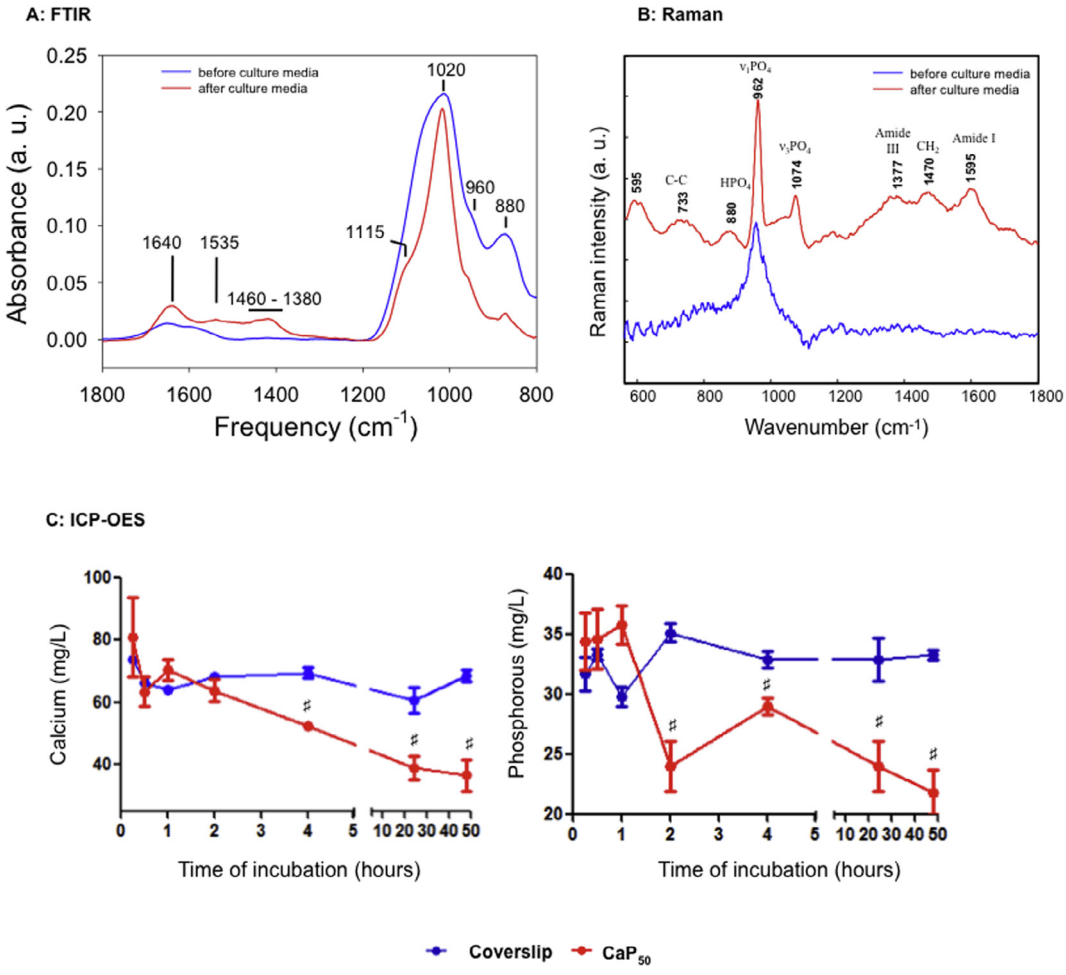

Fig. 2. Bioactivity of calcium phosphate substrate. A: Spectra obtained by Fourier Transform Infrared Spectroscopy before (blue line) and after (red line) 24 h of incubation in serum-containing DMEM. B: Spectra obtained by Raman Spectroscopy before (blue line) and after (red line) 24 h of incubation in serum-containing DMEM. C. Graphs of concentrations of calcium and phosphorous ions in serum free-DMEM analysed by ICP-OES (# CaP_{50} versus coverslip glass $p < 0.01$). (For interpretation of the references to colour in this figure legend, the reader is referred to the web version of this article.)

collagenous polymers are used as barrier membranes and are desired to have matching mechanical properties with bone [28]. For orthopaedic applications, CaPs are used as coatings on titanium and titanium alloy implants to combine the bioactivity of the CaP and the strength of the metal [29,30]. In this case, thin CaP coatings with less than 10 μm are favoured because of their uniformity; in structure and composition, and their greater stability in the biological environment [31]. In this study, coating both of titanium and polymeric membrane was successfully achieved (data not shown). A deeper characterisation of CaP coating of titanium and polymeric membrane would need other investigations (Table 2).

3.2. Cell behaviour on CaP

Perinatal stem cells became an alternative to embryonic and adult stem cells in regenerative medicine. WJ-SCs are more primitive cells compared to adult SCs [5,32]. Our data are in full agreement with this notion as we detected both multipotent antigenic markers (CD73, CD90, CD105, CD44) and pluripotent transcriptomic stem cell markers (POU5F1, SOX2 and hTERT) [17]. In this work, we investigated if WJ-SCs could be considered as sensitive and versatile cellular model in the monitoring of the biocompatibility and osteoinductive properties of sprayed CaP.

Cell behaviour is responsive to physical features of the substrate, and the way cells adhere and spread on the surface influences their morphology, growth, and differentiation [8,9]. CaP constituted by 100 and 150 spray cycles prevent cell attachment. In addition to the substrate instability in culture media, and considering their physico-chemical features, the higher roughness of CaP_{100} and CaP_{150} could decrease the contact area between the cell membrane and the surface inducing a greater cellular stress compared to CaP_{50} [33]. Thus, the further part of the study is only focused on the CaP_{50} substrate, which allowed us to investigate the physical cues of the substrate on WJ-SCs behaviour. Indeed, based on ICP-OES results, the decrease of calcium and phosphorus ions in culture medium allowed us to eliminate the influence of both ions, which has previously been shown to promote bone healing [25]. After five days of culture, WJ-SCs response to the CaP_{50} is observed by AFM to determine WJ-SCs morphology and stiffness and by fluorescent microscopy after labelling cytoskeleton (F-actin) and vinculin. A dramatic change in WJ-SCs morphology and mode of adhesion are observed on CaP_{50}. Most of cells on CaP_{50} organized themselves in small colonies (Fig. S2 supporting information), with greater and apparent cytoplasmic extensions and filopodial attachments whereas on the glass (control) cells kept their fibroblastic morphology (Fig. 4A). F-actin stress fibers of WJ-SCs cultured on CaP_{50} were oriented perpendicularly to each other in contrast to the control where fibers were parallel to the longitudinal WJ-SCs axis (Fig. 4B). Both cytoplasmic and focal adhesion complex vinculin are stained.

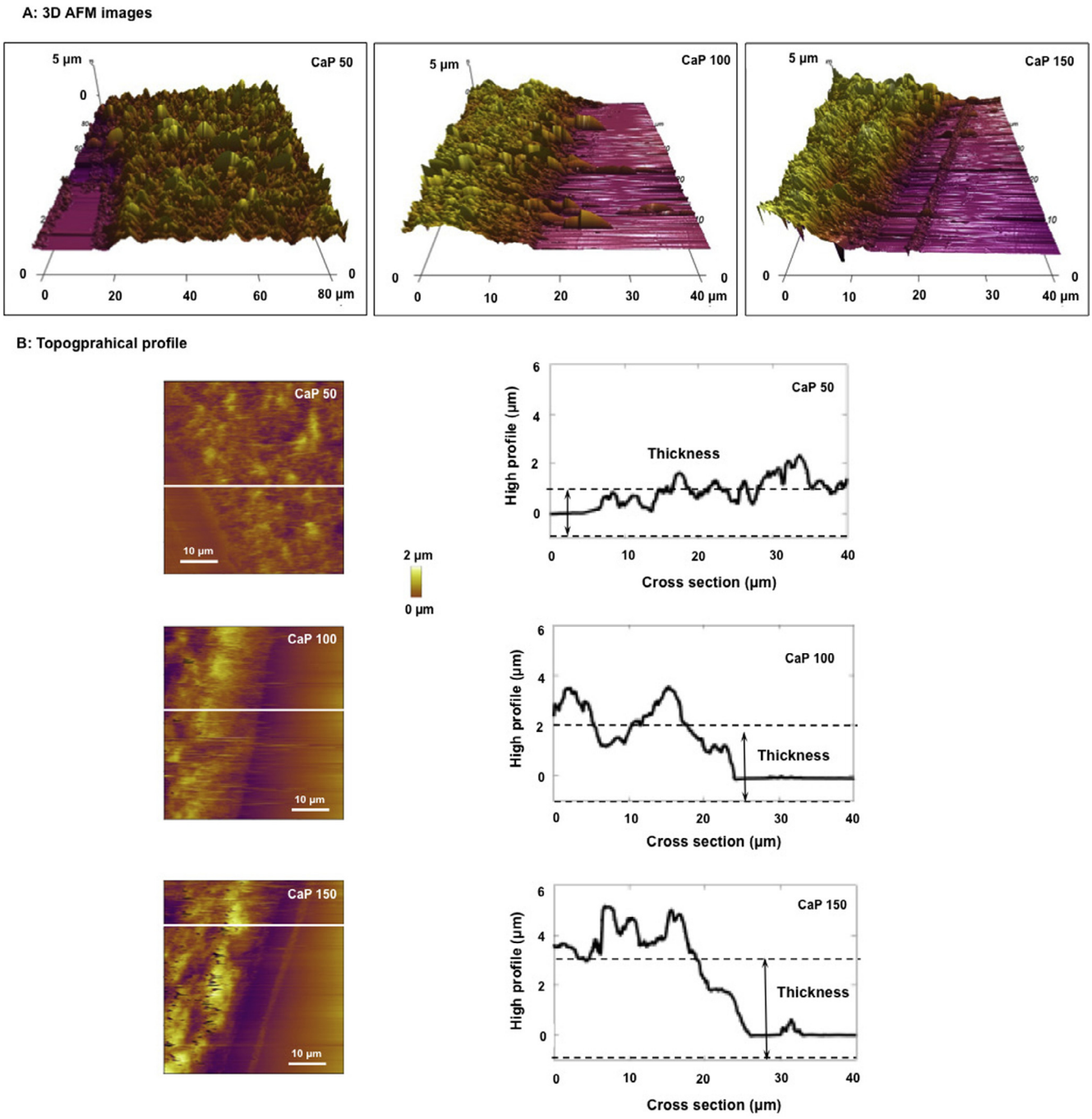

Fig. 3. Roughness and stiffness of CaP substrate. A: Representative atomic force microscopy three dimensional map of CaP substrates. B: The white lines on AFM images indicate the cross-sectional direction adopted in profile analysis. Cross-sections at the level of the scratched zone showing the difference between the upper and lower zones of heights.

Discernable and prominent vinculin abundantly clustered at the extreme ends of the cell body was observed on CaP_{50} (Fig. 4B square). In contrast, vinculin was evenly distributed throughout the cell body on glass substrate (Fig. 4B arrows). The rearrangement of mechanosensitive vinculin at the extreme ends of the cell body, in response to substrate topography, strengthens cell adhesion [34]. Its recruitment to focal adhesions is regulated by externally- or internally-generated mechanical forces whereas its stabilisation is reinforced when vinculin is under tension [35]. To evaluate this effect, the mechanical properties of single WJ-SCs cultivated for five days are determined by AFM nano-indentation experiments.

Even though WJ-SCs were fixed, we observed an elastic modulus ≈18.5 ± 8.2 kPa of cells growing on CaP_{50}, which is nearly 2.25-fold higher than WJ-SCs growing on glass (Fig. 4C). The stiffness distribution, centered at 8.7 ± 2.5 kPa, is relatively broad on the glass coverslip with 55% of the stiffness values lower than 25 kPa. The stiffness values greater than 50 kPa should correspond to thin areas of elongated cells and also should reflect the presence of thin extracellular matrix. The indentation measurements performed on samples with low thicknesses are more sensitive to the presence of the hard glass substrate, *i.e.* to the Young modulus and thus leading to higher apparent stiffness. The stiffness result agrees with the hypothesis that cytoskeleton rearrangement and

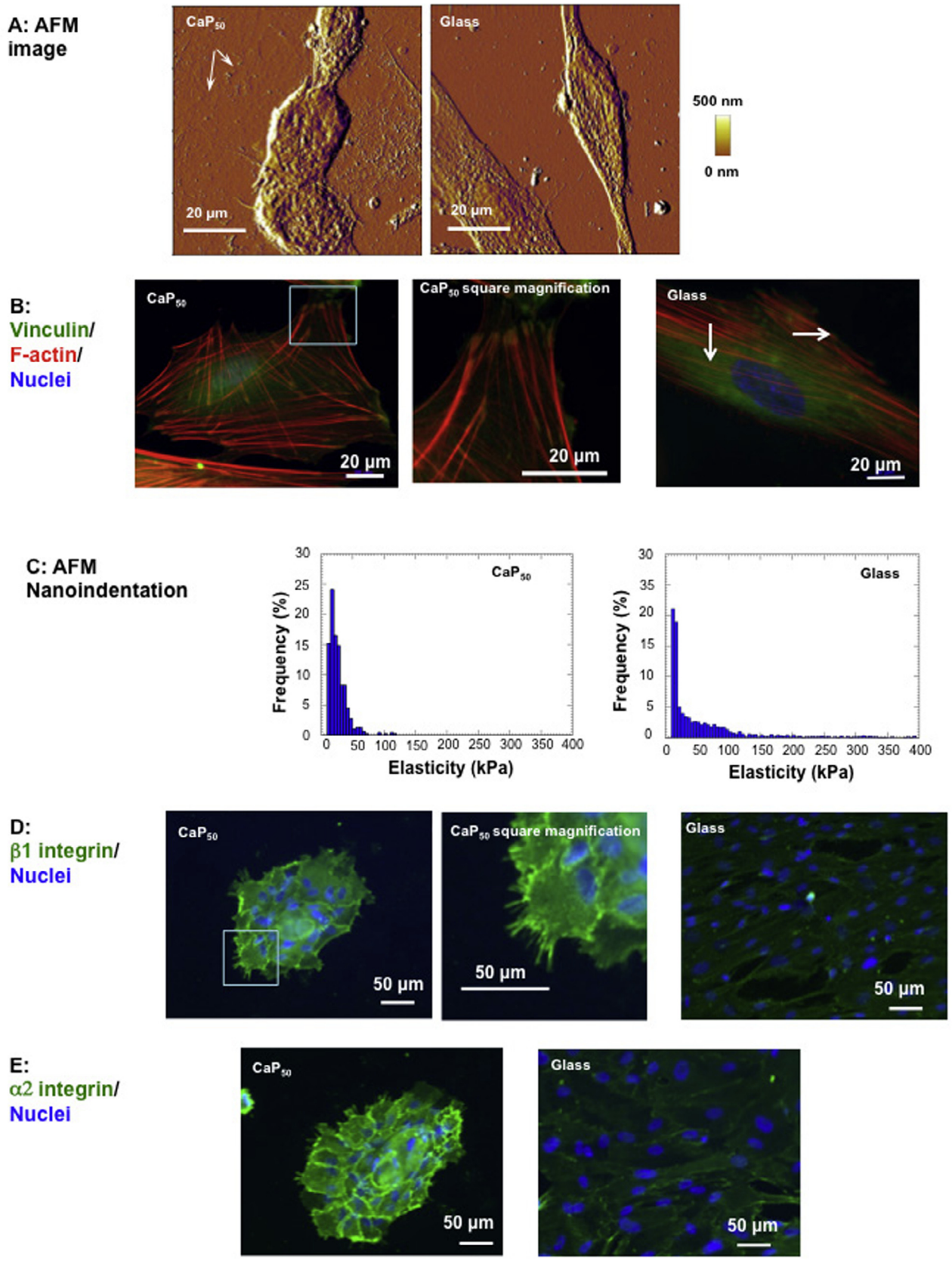

Fig. 4. Wharton's jelly stem cell behaviour at short time culture. WJ-SCs cultured on calcium phosphate (CaP_{50}) and on coverslip for five days were analysed by AFM (A and C) and fluorescent microscopy (B, D and E). A: AFM deflexion images showing polygonal cells on CaP_{50} and fibroblastic cells on coverslip (white arrows indicate neo-synthetized ECM fibers). B: fluorescent images of F-actin (red colour) and of vinculin (green colour) co-staining, highlighting the formation of focal adhesion on CaP_{50} (square). White arrows indicate peri-nuclear distribution of vinculin on control. C: Statistic distribution of the elastic modulus corresponding to 2D map in (A) showing stiff WJ-SCs on CaP_{50} compared to glass. Stiffness histograms were generated from 3×2500 mechanical measurements. For each samples, three force volume images of 2500 force curves were recorded at different location over 6400 μm^2 surface areas. D and E: Fluorescent images of $\alpha 2/\beta 1$ integrin (green colour) on CaP_{50} showing cell-cell and cell-ECM contact distribution. Square indicates filopodia. (For interpretation of the references to colour in this figure legend, the reader is referred to the web version of this article.)

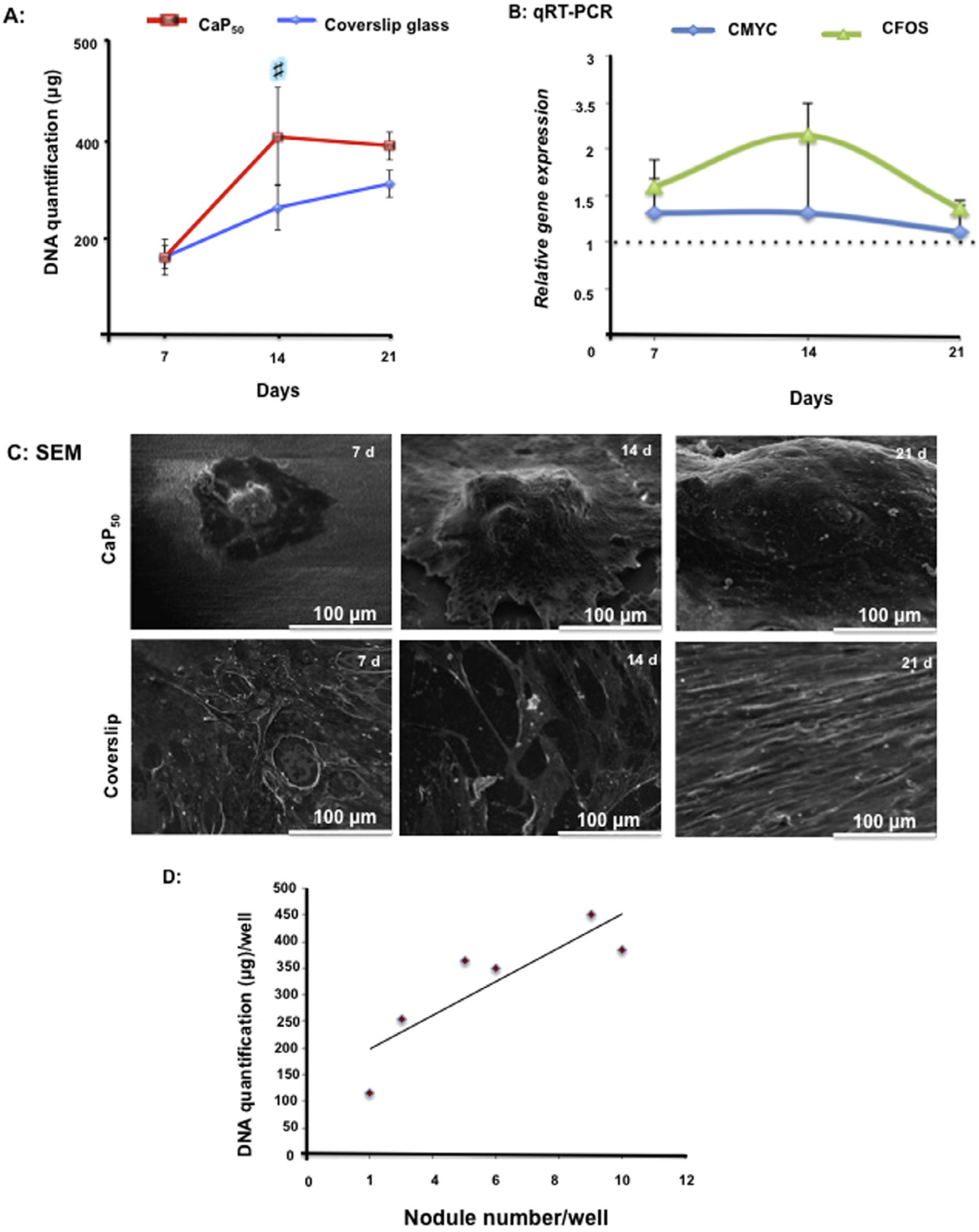

Fig. 5. Wharton's jelly stem cell behaviour at long time of culture. WJ-SCs cultured on calcium phosphate (CaP_{50}) and on coverslip for 7, 14 and 21 days were analysed through DNA content, qRT-PCR and SEM visualization. A: DNA quantification of WJ-SCs over time of study showing high DNA content on CaP_{50} compared to glass. B: CMYC and CFOS mRNA relative expression. The black dashed line indicates the gene expression level of the reference group (coverslip). C: Representative SEM images (at upper row) showing cell accretions on $CaP_{50,}$ which increase in size over time and cellular layer on the coverslip (lower row) (scale bar 100 µm). D: 21 days after culture, cell accretions were manually counted. The number of nodule increased in relation to DNA content per well. Results represented by mean ± SEM, provided from six different donors and each sample was run in duplicate. (# CaP_{50} versus coverslip glass $p < 0.01$).

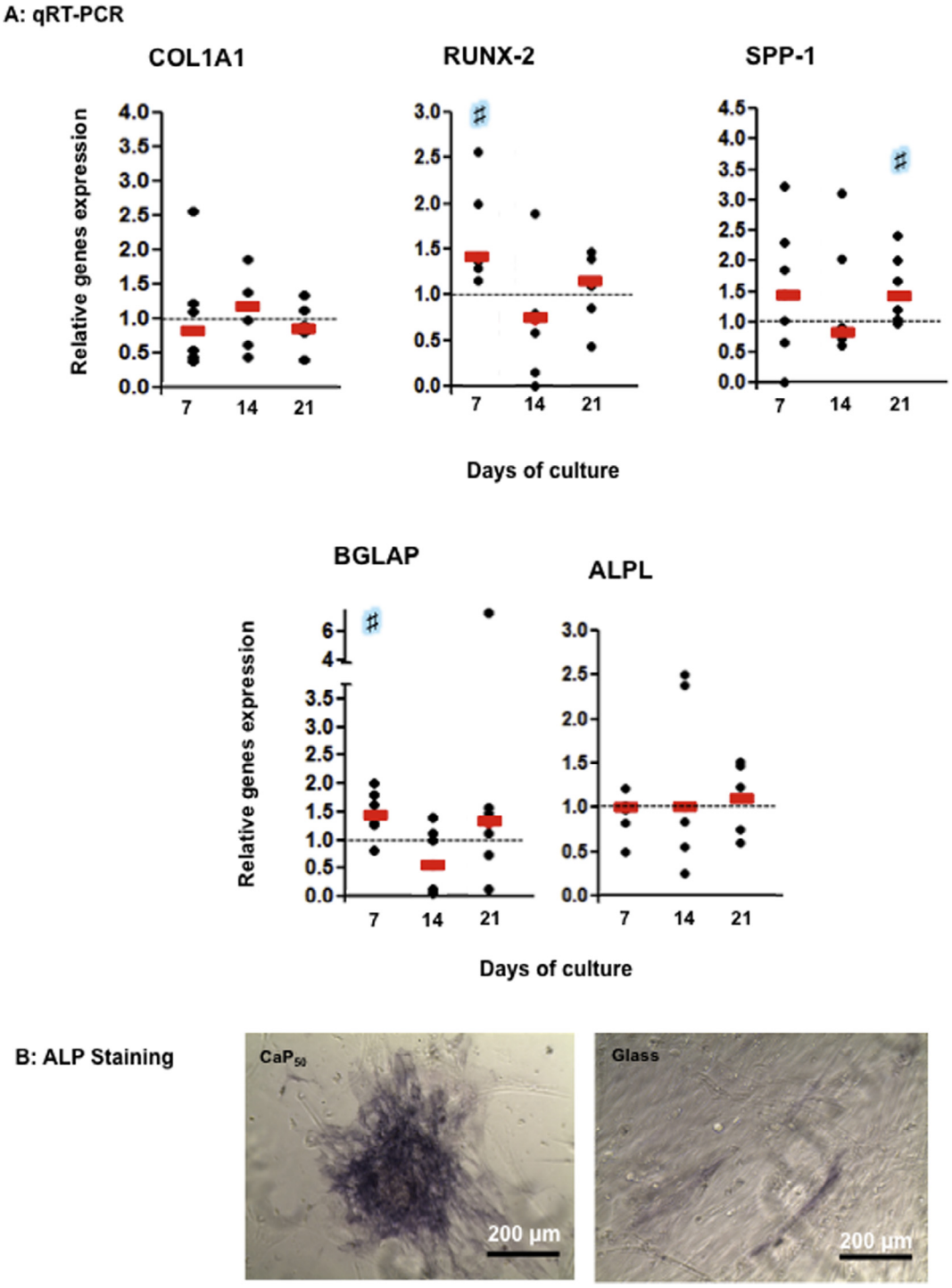

Fig. 6. Osteoblastic characterization. WJ-SCs cultured on calcium phosphate (CaP_{50}) and on coverslip for 7, 14 and 21 days were analysed through the expression of osteoblastic markers by qRT-PCR. A: Relative expression of genes involved in skeletal development [COL1A1 (for type I collagen), Runx-2 (for Transcription factor) and Spp-1 (for osteopontin)] represented on upper line and genes involved in bone mineralization [BGLAP (for osteocalcin) and ALPL (for Alkaline phosphatase)] represented on second line. The black dashed line indicates the gene expression level of the reference group (glass). Results represented by median (red bars), provided from six different donors and each sample was run in duplicate. (# CaP_{50} *versus* coverslip glass $p < 0.05$). B: 14-days old nodule positive for alkaline phosphatase staining (scale bar 200 µm).

vinculin recruitment to the focal adhesion increase the stiffness of cells. To further elucidate how stimulation by CaP_{50} was transduced across cell membranes into WJ-SCs and affected the formation of cell colonies, we analysed the expression of α2 and β1 integrin subunits, which either have a high collagen-binding affinity or are essential for mechanosensing and mechanotransduction [36,37]. WJ-SCs colonies expressed strongly both α2 and β1 integrin subunits. Labelled integrins are restricted to cell-cell and cell-substrate contacts (Fig. 4D and E). In our experiments, the higher expression of α2/β1 on CaP_{50} may be related to the synthesis and the assembly of type I collagen (COL-1) within the secreted extracellular matrix (Fig. 4A arrows). Based on these results, we conclude that WJ-SCs adhere strongly to CaP_{50} with a well-developed filopodia. Although the mechanisms involved are not

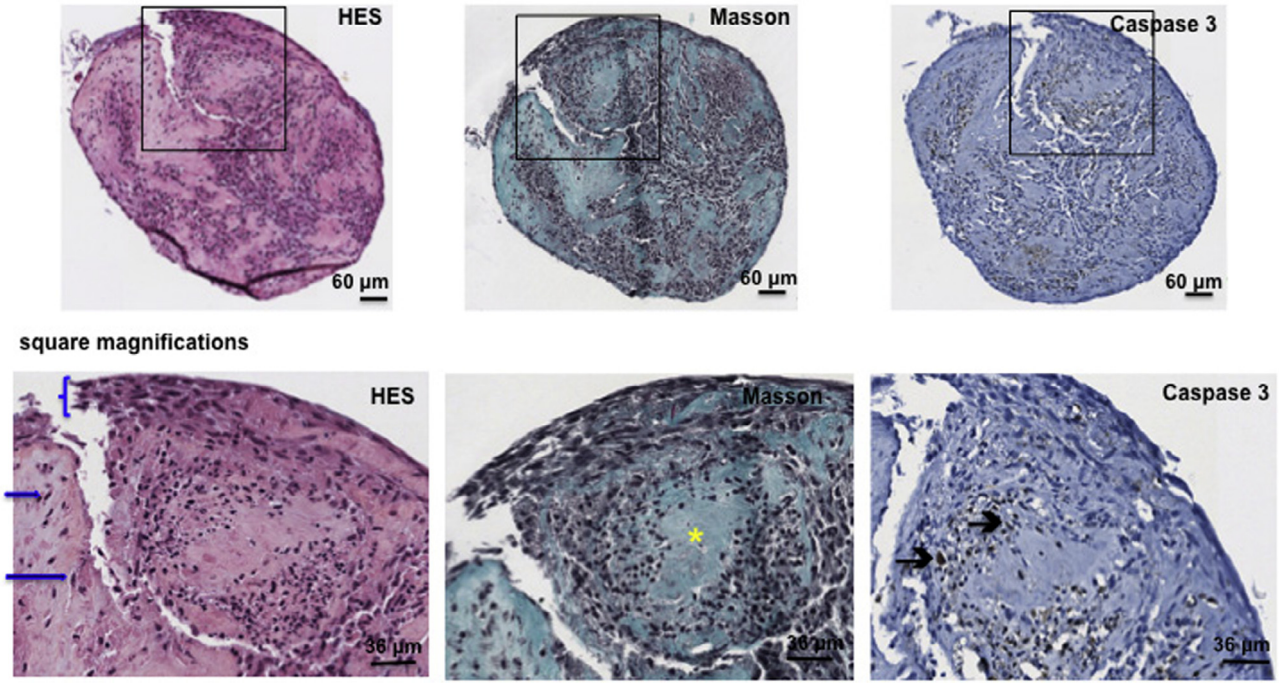

Fig. 7. Histological characterization of 28-day old nodules. WJ-SCs cultured on calcium phosphate (CaP_{50}) for 28 days were embedded in paraffin, cut into 4 µm sections and face view-sections (parallel to the culture substrate) were stained. HES staining, showing nuclei in blue and cells in pink. High magnification indicating multilayered cells at the surface of the nodule (curly blue bracket) and randomly distributed cells embedded within fibrous tissues (blue arrows). Masson's trichrome, showing nuclei in brown, cytoplasm in dark and collagen in green. High magnification confirming randomly distributed cells embedded within collagenous matrix (yellow star). Clived-caspase 3 immunostaining showing few apoptotic cells within fibrous tissues (black arrows). (Scale bars 60 µm and 38 µm). (For interpretation of the references to colour in this figure legend, the reader is referred to the web version of this article.)

clearly established, we can speculate that a reorganization of the actin cytoskeleton and an increase of stiffness of WJ-SCs on CaP_{50} could be related to the responsiveness of these cells to the physical cues such as nano-scale structure and stiffness of the sprayed substrate [38].

3.3. Osteogenic commitment of stem cells on CaP

Bone regeneration represents a well-orchestrated series of biological events of SCs recruitment, proliferation and differentiation that can be recapitulated *in vitro* through the formation of three-dimensional structures usually called bone-*like* nodules. The next experiment is designed to follow the model of osteoblastic differentiation described by Aubin and Heersche [39] and by Gentleman et al. [40]. In osteogenic regeneration, the desired outcome would be an osteoinductive substrate that would not require any additional growth factors to promote SCs differentiation [25]. Thus, our experiments were carried out without any additional osteogenic factors [6]. We first monitored kinetics of the cell proliferation through measurement of the DNA content and the modulation of cell cycle regulator genes as CMYC and CFOS. When WJ-SCs are cultivated on CaP_{50}, DNA content increased more rapidly with a plateau appearing from day 14 until day 21 whereas on the glass control, DNA increased linearly from day 7 to 21 (Fig. 5A). WJ-SCs up-regulated CFOS mRNA at 14 days whereas CMYC mRNA is slightly regulated compared to control (Fig. 5B). The CFOS regulation, an early gene response identified during the developmental stages [41], reinforces the hypothesis that CaP_{50} features can favour osteoblast commitment. Over 6 days, significant changes in growth patterns of WJ-SCs on CaP_{50} and glass were apparent. Indeed, SEM observations showed nodule structures on CaP_{50} whereas WJ-SCs cultured on glass formed confluent monolayer (Fig. 5C). These nodule structures arose from WJ-SCs colonies described above. These observations agree with the data presented by Gentleman et al., describing that bone-*like* nodules arise directly from embryonic SCs in contrast to OBs and adult SCs which form bone-*like* nodules from colonies formation and cellular aggregation [40]. While previous reports have shown that the increase in size of the bone-*like* nodule arise from ECM deposition [42], in our study time laps monitoring showed a fusion of the nodules (Video in supplementary data SI). The number of nodules was found to be proportional to DNA quantity (Fig. 5D), illustrating that cell number could affect the increase of the size of the nodule. The size of WJ-SC derived dense cellular structure was about 100 µm at day 7 and 600 µm at day 21. In the literature, the initial cell density of bone-*like* nodules varies from 5 to 35 cells per nodule and its size and thickness increase during the course of differentiation. 20-day-old nodules comprise approximately 100 cells per nodule, with a thickness of 70–100 µm [43]. We next investigated the expression of genes expected to be regulated during osteogenic commitment. We focused our attention on genes involved in bone development (COL1A1, RUNX-2, SPP-1) and mineralization (BGLAP, ALPL) (Fig. 6A). Our results demonstrated that COL1A1 is up-regulated at 14 days of culture. RUNX-2 and SPP-1 (early markers of osteoblast differentiation) are up-regulated at day 7 (with $p < 0.05$ for RUNX-2) and day 21 (with $p < 0.05$ for SPP-1). Among bone mineralization genes, the changes in BGLAP expression over time are noteworthy. Its mRNA expression peaked on day 7 ($p < 0.05$) and day 21. Alkaline phosphatase (ALP) is recognized as one of the key player in the early stage of matrix mineralization. Its major function consists in hydrolysis of inorganic pyrophosphate [44]. While ALPL was not regulated over the time, ALP staining was detected when cells are grown on CaP_{50} after 14 days of culture (Fig. 6B). No change in ALP staining pattern was observed between 14 and 21 days of culture. Although ALPL results are consistent with the previous

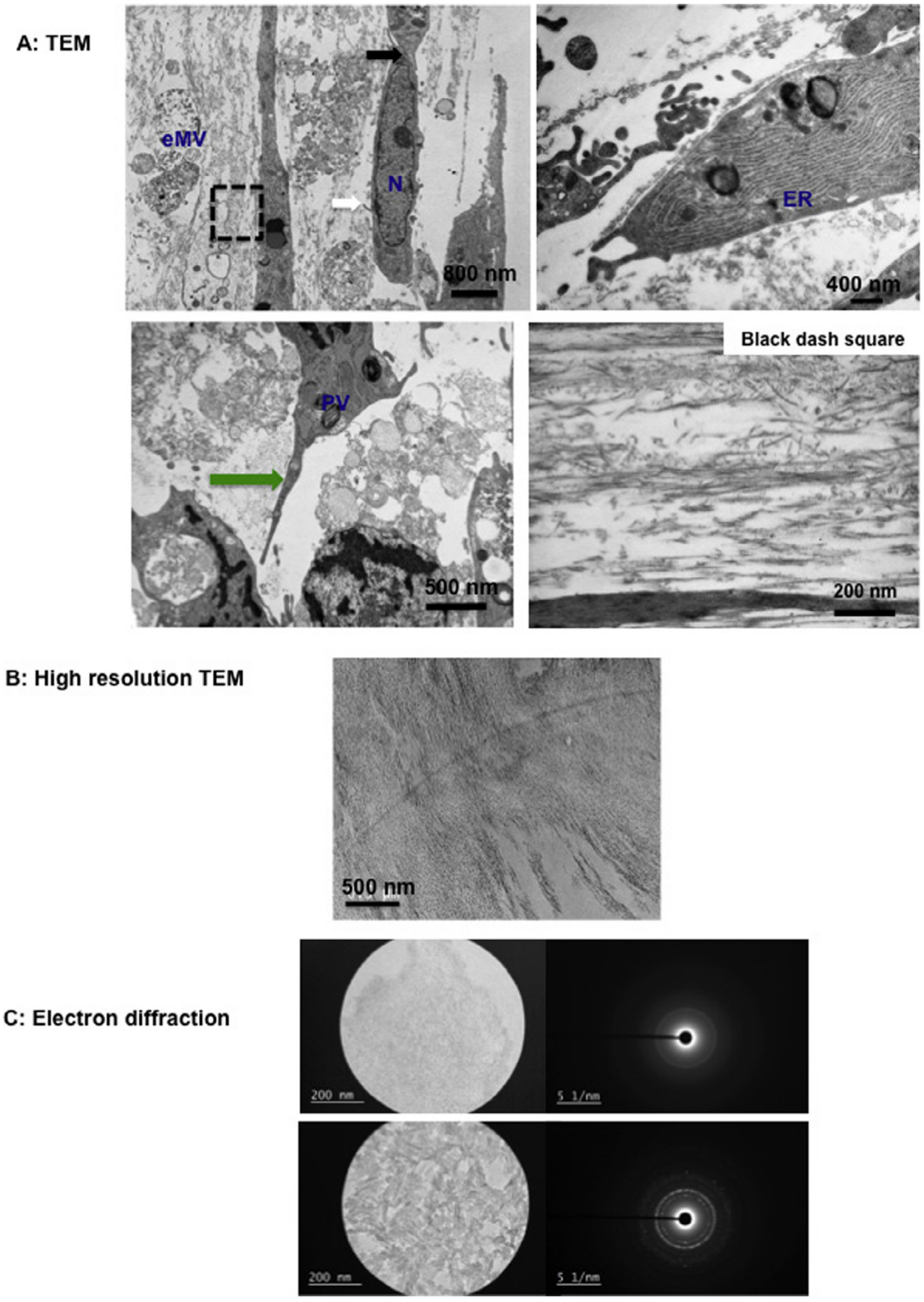

Fig. 8. Ultrastructural characterization of 28-day old nodules. WJ-SCs cultured on calcium phosphate (CaP_{50}) for 28 days were embedded in resin and cut into ultrathin sections. Perpendicular sections (to the culture substrate) were examined by transmission electron microscopy and analysed by electron diffraction. A: Representative TEM images showing cells with a developed network of rough endoplasmic reticulum and numerous vesicles, cellular junctions (black arrow) and a cilia-like structure (white arrow in upper picture). Dipper localized cells showing prominent membrane extensions through the ECM (green arrow, lower left picture). Black dashed square showing type I collagen fibers (lower right picture) [eMV = extracellular matrix vesicles, N = nucleus, ER = endoplasmic reticulum, PV = phagozome vesicles]. B: High-resolution TEM of the crystal-like structure that can be light or dense. C: electron diffraction.

published work [45], we hypothesis that the inter-individual responses of SCs due to heterogeneity and donor number (>6) are thought to be responsible for the absence of significant regulation of ALPL mRNA.

3.4. Nodule characterization

Bone formation is a multistep process starting by gene expression of osteoblasts leading to protein synthesis and formation of an

osteoid (*i.e.* COL-I fibers and apatite minerals). Following a period of secretory activity, osteoblasts undergo either apoptosis or terminal differentiation to form osteocytes surrounded by bone matrix [46]. A general overview about nodule up to 28 days of culture on CaP_{50} is given by hematoxylin-eosin-Saffran (HES) and Masson's trichrome staining. Observation of histological face view-sections of the upper surface (uppermost side exposed to culture medium) revealed continuous layers of cells at the surface of the nodule (Fig. 7 curly bracket) with randomly distributed cells embedded within fibrous tissues (Fig. 7 blue arrows). Masson's trichrome stain confirmed the presence of green-stained fibrous tissue composed of newly formed collagen (Fig. 7, yellow asterisk). Apoptotic cells positive to cleaved caspase 3 immunohistochemistry are also detected in the inner region of the nodule (Fig. 7, black arrows), suggesting that the programmed cell death may provide a mechanism for regulating the cell number of osteoblast-*like* that further differentiate into osteocytes-*like*.

Most reports state that successful OBs commitment occurs when the produced ECM is positive to alizarin red or *von Kossa* staining, but conclusions drawn from these works may not have physiological relevance to bone formation (*i.e.,* dystrophic minerals from culture media or necrotic promoting inappropriate mineralization) and mineralization as it occurs *in vivo* [47–50]. To perform a comprehensive structural and compositional characterization of bone-*like* nodule, we investigated the mineralization of the nodule by using transmission electron microscopy (TEM), high resolution-TEM and electron diffraction (the benchmark "gold standard" technique for the determination of crystal structure for any given mineral). TEM examinations of perpendicular sections of 28-day old nodule revealed multilayered structures containing cells that are interconnected by gap junctions and cell processes (Fig. 8A). Two distinct populations of cells are identified. First, osteoblast-*like* cells, with a round nucleus and well-developed network of rough endoplasmic reticulum and numerous vesicles, membrane protrusions at their upper plasma membrane and tight junctions between adjacent cells (Fig. 8A, black and white arrows). Secondly, osteocyte-*like* cells with an elongated and large nucleus, reduced organelles and some autophagosomes (Fig. 8A). Osteocyte-*like* cells embedded within matrix showed prominent membrane extensions through the ECM (Fig. 8A green arrow) similar to those seen in bone *in vivo* [51]. While *in vitro* studies reported that without exposure to ascorbic acid, osteoblast fails to externalize and assemble the type I collagen network [52], the ECM of the formed nodule (in absence of ascorbic acid) is mainly composed of collagen which by TEM displayed the characteristic 67 nm banding periodicity typical of COL I fibrils (Fig. 8A black square). At high-TEM magnification, it is possible to observe electron-dense platelets (Fig. 8B). Larger crystals of the central area are surrounded by shell made of tiny crystallites. Both crystalline structures are identified as hydroxyapatite using electron diffraction analysis (Fig. 8C). Based on TEM observations, it can be argued that WJ-SCs growing on CaP_{50} self-assemble into a 3D structure and create a mineralized collagenous matrix. In our study, it is important to note that the bone *like*-nodules formed from WJ-SCs are due to the intrinsic substrate properties and not the result of soluble osteogenic supplements as previously reported [39,40].

In the past few decades, one of the important achievements was the development of materials (3D scaffolds and coating) with intrinsic osteoinductivity [7]. Inherent osteoinductive property due to the macrostructure [53] or combined with osteoinductive drugs as BMP-2 [54] have been reported. All the above-mentioned studies focused on the *in vivo* characterisation of CaP osteoinductive properties. Until now, there is a lack of knowledge on stem cell behaviour on CaP materials. Herein, sprayed biomimetic solutions using mild conditions led to the formation of CaP coating with controlled physical properties, good bioactivity, and biocompatibility. Our study shows, for the first time, that *via* optimization of physical properties, the CaP substrate could induce osteogenic differentiation of perinatal stem cells without adding any osteogenic factors. Thus, sprayed CaP represents a simple and novel approach for surface functionalization with a controllable nano-roughness for bone regeneration and repair.

Declaration of interest

The manuscript was written through contributions of all authors. All authors have given approval to the final version of the manuscript. The authors declare that they have no competing interests.

Acknowledgments

The authors are very grateful to the staff of Reims Maternity Hospital for providing umbilical cords and the staff of the Core URCACyt and PICT (URCA). This work was partially supported by IMACELL from CNRS project, France. S. Mechiche Alami was supported by a doctoral fellowship of la ville de Reims. We thank E. Mathieu from INSERM U1121 (Université de Strasbourg, France) for technical help concerning transmission electron microscopy, N. Bouland for technical help concerning histology, Dr. S. Audonnet for cytometry analysis, Dr. A. Beljebbar for Raman spectroscopy analysis and Dr. S. Sayan for ICP.

Appendix A. Supplementary data

Supplementary data associated with this article can be found, in the online version, at http://dx.doi.org/10.1016/j.actbio.2016.11.042.

References

[1] S. Scarfì, Use of bone morphogenetic proteins in mesenchymal stem cell stimulation of cartilage and bone repair, World J. Stem Cells 8 (2016) 1–12.
[2] A.S. Curry, N.W. Pensa, A.M. Barlow, S.L. Bellis, Taking cues from the extracellular matrix to design bone-mimetic regenerative scaffolds, Matrix Biol. 52–54 (2016) 397–412.
[3] C.T. Vangsness Jr., H. Sternberg, L. Harris, Umbilical cord tissue offers the greatest number of harvestable mesenchymal stem cells for research and clinical application: a literature review of different harvest sites, Arthrosc. J. Arthrosc. Relat. Surg. 31 (2015) 1836–1843.
[4] T. Nagamura-Inoue, H. He, Umbilical cord-derived mesenchymal stem cells: their advantages and potential clinical utility, World J. Stem Cells 6 (2014) 195–202.
[5] J.W. Si, X.D. Wang, S.G. Shen, Perinatal stem cells: a promising cell resource for tissue engineering of craniofacial bone, World J. Stem Cells 7 (2015) 149–159.
[6] F. Langenbach, J. Handschel, Effects of dexamethasone, ascorbic acid and β-glycerophosphate on the osteogenic differentiation of stem cells in vitro, Stem Cell Res. Ther. 4 (2013) 117.
[7] R.Z. LeGeros, Calcium phosphate-based osteoinductive materials, Chem. Rev. 108 (2008) 4742–4753.
[8] W.L. Murphy, T.C. McDevitt, A.J. Engler, Materials as stem cell regulators, Nat. Mater. 13 (2014) 547–557.
[9] M.J. Dalby, N. Gadegaard, R.O.C. Oreffo, Harnessing nanotopography and integrin-matrix interactions to influence stem cell fate, Nat. Mater. 13 (2014) 558–569.
[10] R. Bosco, E.R. Urquia Edreira, J.G.C. Wolke, S.C.G. Leeuwenburgh, J.J.J.P. van den Beucken, J.A. Jansen, Instructive coatings for biological guidance of bone implants, Surf. Coat. Technol. 233 (2013) 91–98.
[11] R.A. Surmenev, M.A. Surmeneva, A.A. Ivanova, Significance of calcium phosphate coatings for the enhancement of new bone osteogenesis – a review, Acta Biomater. 10 (2014) 557–579.
[12] G. Popa, F. Boulmedais, P. Zhao, J. Hemmerlé, L. Vidal, E. Mathieu, O. Félix, P. Schaaf, G. Decher, J.C. Voegel, Nanoscale precipitation coating: the deposition of inorganic films through step-by-step spray-assembly, ACS Nano 4 (2010) 4792–4798.
[13] F. Velard, S. Schlaubitz, J.C. Fricain, C. Guillaume, D. Laurent-Maquin, J. Möller-Siegert, L. Vidal, E. Jallot, S. Sayen, O. Raissle, J.M. Nedelec, C. Vix-Guterl, K. Anselme, J. Amédée, P. Laquerrière, In vitro and in vivo evaluation of the inflammatory potential of various nanoporous hydroxyapatite biomaterials, Nanomedicine 10 (2015) 785–802.

[14] I.N. Sneddon, The relation between load and penetration in the axisymmetric boussinesq problem for a punch of arbitrary profile, Int. J. Eng. Sci. 3 (1965) 47–57.
[15] N. Gavara, R.S. Chadwick, Determination of the elastic moduli of thin samples and adherent cells using conical atomic force microscope tips, Nat. Nanotechnol. 7 (2012) 733–736.
[16] P. Polyakov, C. Soussen, J. Duan, J.F.L. Duval, D. Brie, G. Francius, Automated force volume image processing for biological samples, PLoS One 6 (2011) e18887.
[17] S. Mechiche Alami, F. Velard, F. Draux, F. Siu Paredes, J. Josse, F. Lemaire, S.C. Gangloff, O. Graesslin, D. Laurent-Maquin, H. Kerdjoudj, Gene screening of Wharton's jelly derived stem cells, Biomed. Mater. Eng. 24 (2014) 53–61.
[18] W. Habraken, P. Habibovic, M. Epple, M. Bohner, Calcium phosphates in biomedical applications: materials for the future?, Mater Today 19 (2016) 69–87.
[19] E. Beniash, Biominerals-hierarchical nanocomposites: the example of bone, Wiley Interdiscip. Rev. Nanomed. Nanobiotechnol. 3 (2011) 47–69.
[20] M.D. Grynpas, S. Omelon, Transient precursor strategy or very small biological apatite crystals?, Bone 41 (2007) 162–164
[21] P.A. Ngankam, P. Lavalle, J.C. Voegel, L. Szyk, G. Decher, P. Schaaf, F.J.G. Cuisinier, Influence of polyelectrolyte multilayer films on calcium phosphate nucleation, J. Am. Chem. Soc. 122 (2000) 8998–9005.
[22] S.J. Gadaleta, E.P. Paschalis, F. Betts, R. Mendelsohn, A.L. Boskey, Fourier transform infrared spectroscopy of the solution-mediated conversion of amorphous calcium phosphate to hydroxyapatite: new correlations between X-ray diffraction and infrared data, Calcif. Tissue Int. 58 (1996) 9–16.
[23] S. Mandel, A.C. Tas, Brushite ($CaHPO_4{\cdot}2H_2O$) to octacalcium phosphate ($Ca_8(HPO_4)_2(PO_4)_4{\cdot}5H_2O$) transformation in DMEM solutions at 36.5 °C, Mater. Sci. Eng. C 30 (2010) 245–254.
[24] G.S. Mandair, M.D. Morris, Contributions of Raman spectroscopy to the understanding of bone strength, BoneKEy Rep. 4 (2015) 1–8.
[25] E.S. Place, N.D. Evans, M.M. Stevens, Complexity in biomaterials for tissue engineering, Nat. Mater. 8 (2009) 457–470.
[26] A. Hoppe, N.S. Güldal, A.R. Boccaccini, A review of the biological response to ionic dissolution products from bioactive glasses and glass-ceramics, Biomaterials 32 (2011) 2757–2774.
[27] X. Wang, S. Xu, S. Zhou, W. Xu, M. Leary, P. Choong, M. Qian, M. Brandt, Y.M. Xie, Topological design and additive manufacturing of porous metals for bone scaffolds and orthopaedic implants: a review, Biomaterials 83 (2016) 127–141.
[28] E.J. Lee, D.S. Shin, H.E. Kim, H.W. Kim, Y.H. Koh, J.H. Jang, Membrane of hybrid chitosan-silica xerogel for guided bone regeneration, Biomaterials 30 (2009) 743–750.
[29] F. Barrere, C.A. van Blitterswijk, K. de Groot, P. Layrolle, Influence of ionic strength and carbonate on the Ca-P coating formation from SBFx5 solution, Biomaterials 23 (2002) 1921–1930.
[30] F. Barrère, C.M. van der Valk, R.A.J. Dalmeijer, C.A. van Blitterswijk, K. de Groot, P. Layrolle, In vitro and in vivo degradation of biomimetic octacalcium phosphate and carbonate apatite coatings on titanium implants, J. Biomed. Mater. Res. A 64A (2003) 378–387.
[31] B. Leon, J.A. Jansen, Thin Calcium Phosphate Coatings for Medical Implants, Springer, 2009. URL <http://link.springer.com/book/10.1007/978-0-387-77718-4>.
[32] D.C. Ding, Y.H. Chang, W.C. Shyu, S.-Z. Lin, Human umbilical cord mesenchymal stem cells: a new era for stem cell therapy, Cell Transplant. 24 (2015) 339–347.
[33] B.D. Boyan, A. Cheng, R. Olivares-Navarrete, Z. Schwartz, Implant surface design regulates mesenchymal stem cell differentiation and maturation, Adv. Dent. Res. 28 (2016) 10–17.
[34] R.J. McMurray, N. Gadegaard, P.M. Tsimbouri, K.V. Burgess, L.E. McNamara, R. Tare, K. Murawski, E. Kingham, R.O.C. Oreffo, M.J. Dalby, Nanoscale surfaces for the long-term maintenance of mesenchymal stem cell phenotype and multipotency, Nat. Mater. 10 (2011) 637–644.
[35] C. Grashoff, B.D. Hoffman, M.D. Brenner, R. Zhou, M. Parsons, M.T. Yang, M.A. McLean, S.G. Sligar, C.S. Chen, T. Ha, M.A. Schwartz, Measuring mechanical tension across vinculin reveals regulation of focal adhesion dynamics, Nature 466 (2010) 263–266.
[36] X. Wang, Z. Schwartz, R.A. Gittens, A. Cheng, R. Olivares-Navarrete, H. Chen, B. D. Boyan, Role of integrin $\alpha2\beta1$ in mediating osteoblastic differentiation on three-dimensional titanium scaffolds with submicron-scale texture, J. Biomed. Mater. Res. A 103 (2015) 1907–1918.
[37] M. Lai, C.D. Hermann, A. Cheng, R. Olivares-Navarrete, R.A. Gittens, M.M. Bird, M. Walker, Y. Cai, K. Cai, K.H. Sandhage, Z. Schwartz, B.D. Boyan, Role of $\alpha2\beta1$ integrins in mediating cell shape on microtextured titanium surfaces, J. Biomed. Mater. Res. A 103 (2015) 564–573.
[38] G.D. Pemberton, P. Childs, S. Reid, H. Nikukar, P.M. Tsimbouri, N. Gadegaard, A. S.G. Curtis, M.J. Dalby, Nanoscale stimulation of osteoblastogenesis from mesenchymal stem cells: nanotopography and nanokicking, Nanomedicine 10 (2015) 547–560.
[39] J.E. Aubin, J.N.M. Heersche, Osteoprogenitor cell differentiation to mature bone-forming osteoblasts, Drug Dev. Res. 49 (2000) 206–215.
[40] E. Gentleman, R.J. Swain, N.D. Evans, S. Boonrungsiman, G. Jell, M.D. Ball, T.A.V. Shean, M.L. Oyen, A. Porter, M.M. Stevens, Comparative materials differences revealed in engineered bone as a function of cell-specific differentiation, Nat. Mater. 8 (2009) 763–770.
[41] E. Wagner, Functions of AP1 (Fos/Jun) in bone development, Ann. Rheum. Dis. 61 (2002) 40–42.
[42] L. Malaval, F. Liu, P. Roche, J.E. Aubin, Kinetics of osteoprogenitor proliferation and osteoblast differentiation in vitro, J. Cell. Biochem. 74 (1999) 616–627.
[43] S. Mechiche Alami, S.C. Gangloff, D. Laurent-Maquin, Y. Wang, H. Kerdjoudj, Concise Review. In vitro formation of bone-like nodules sheds light on the application of stem cells for bone regeneration, Stem Cells Transl. Med. (2016), http://dx.doi.org/10.5966/sctm.2015-0413.
[44] M. Balcerzak, E. Hamade, Le Zhang, S. Pikula, G. Azzar, J. Radisson, J. Bandorowicz-Pikula, R. Buchet, The roles of annexins and alkaline phosphatase in mineralization process, Acta Biochim. Pol. 50 (2003) 1019–1038.
[45] A.A. Mueller, N. Forraz, S. Gueven, G. Atzeni, O. Degoul, A. Pagnon-Minot, D. Hartmann, I. Martin, A. Scherberich, C. McGuckin, Osteoblastic differentiation of Wharton jelly biopsy specimens and their mesenchymal stromal cells after serum-free culture, Plast. Reconstr. Surg. 134 (2014) 59e–69e.
[46] E.J. Mackie, Osteoblasts: novel roles in orchestration of skeletal architecture, Int. J. Biochem. Cell Biol. 35 (2003) 1301–1305.
[47] S. Boonrungsimana, E. Gentlemana, R. Carzaniga, N.D. Evans, D.W. McComb, A. E. Porter, M.M. Stevens, The role of intracellular calcium phosphate in osteoblast-mediated bone apatite formation, Proc. Natl. Acad. Sci. U.S.A. 109 (2012) 14170–14175.
[48] L.F. Bonewald, S.E. Harris, J. Rosser, M.R. Dallas, S.L. Dallas, N.P. Camacho, B. Boyan, A. Boskey, Von Kossa staining alone is not sufficient to confirm that mineralization in vitro represents bone formation, Calcif. Tissue Int. 72 (2003) 537–547.
[49] N.D. Evans, E. Gentleman, X. Chen, C.J. Roberts, J.M. Polak, M.M. Stevens, Substrate stiffness affects early differentiation events in embryonic stem cells, Eur. Cell. Mater. 18 (2009) 1–14.
[50] J. Silvent, N. Nassif, C. Helary, T. Azais, J.Y. Sire, M.M. Giraud Guille, Collagen osteoid-like model allows kinetic gene expression studies of non-collagenous proteins in relation with mineral development to understand bone biomineralization, PLoS One 8 (2013) e57344.
[51] L.F. Bonewald, The amazing osteocyte, J. Bone Miner. Res. 26 (2011) 229–238.
[52] W.N. Addison, V. Nelea, F. Chicatun, Y.C. Chien, N. Tran-Khanh, M.D. Buschmann, S.N. Nazhat, M.T. Kaartinen, H. Vali, M.M. Tecklenburg, R.T. Franceschi, M.D. McKee, Extracellular matrix mineralization in murine MC3T3-E1 osteoblast cultures: an ultrastructural, compositional and comparative analysis with mouse bone, Bone 71 (2015) 244–256.
[53] H. Yuan, K. Kurashina, J.D. de Bruijn, Y. Li, K. de Groot, X. Zhang, A preliminary study on osteoinduction of two kinds of calcium phosphate ceramics, Biomaterials 20 (1999) 1799–1806.
[54] I. Ono, H. Gunji, K. Suda, F. Kaneko, M. Murata, T. Saito, Y. Kuboki, Bone induction of hydroxyapatite combined with bone morphogenetic protein and covered with periosteum, Plast. Reconstr. Surg. 95 (1995) 1265–1272.